



Bandgap graded perovskite solar cell for above 30% efficiency

J. Lakshmi Prasanna^a, Ekta Goel^a, Amarjit Kumar^a, Amel Laref^b, Chella Santhosh^c, Pranay Ranjan^d, Atul Kumar^{c,*}

^a Department of Electronics and Communication Engineering, National Institute of Technology, Warangal, Telangana, India

^b Physics Department, Faculty of Science, King Saudi University, Riyadh 11451, Saudi Arabia

^c Department of Electronics and Communications Engineering, Koneru Lakshmaiah Education Foundation, Greenfields, Vaddeswaram, Guntur 522502, Andhra Pradesh, India

^d Department of Metallurgical & Materials Engineering, Indian Institute of Technology Jodhpur, Karwar 342037, India

ARTICLE INFO

Keywords:

Index Terms

Band Gap Grading

Perovskite solar cells

SCAPS, SQ limit

ABSTRACT

Perovskite solar cells (PSCs) are deemed to be the upcoming photovoltaic technology with a promise to surpass the silicon solar cell in near future. Herein, we propose a bandgap grading (of 1–3 eV under the effect of stoichiometry variation) profile to maximize the spectrum absorption for the perovskite absorber material, leading to efficiency reaching the Shockley-Queisser (SQ) limit. A comparative study of linear bandgap grading for the different absorber conduction band slope profiles has been analytically performed and analyzed. The bandgaps grading profiles were optimized for device performance, defect tolerances, and optical absorption (quantum efficiency). Accordingly, it has been observed that for optimal efficiency, a high range of bandgap grading is not essential, but rather a well-optimized small range of bandgap grading of 1.4–1.2 eV at the two ends of the absorber layer results in 31% power conversion efficiency.

1. Introduction

Solar energy is a perennial, eco-friendly, free of cost, and omnipresent renewable energy source with abundance surpassing foreseeable demand in energy. [1,2] Perovskite solar cells (PSC) are the potential candidate for large-scale photovoltaics and will possibly replace the existing silicon and GaAs solar cells due to their abundance, better watt/dollar (\$) matrix, and device performance. The ABX₃ PSCs are one of the most promising new generations of solar cells with a performance largely unsusceptible to bulk defects. This has been evident by the astounding increase in the efficiency and performance of perovskite solar cells, from 3.8% in 2009 to 22.1%–25% in 2020. [3–5] This increase in the advancement of the efficiency in PSCs is possible due to the high carrier mobility, optimal absorption coefficient, performance neutral to defects, and wide bandgap tunability of absorber material (better suited to the AM1.5 spectrum). Currently, perovskite solar cells are being investigated with great scientific interest for stabilizing the performance [6] and enhancing the efficiency beyond Shockley Queisser (SQ) limit [7]. PSCs have an inverted planar structure with a configuration of transparent conducting oxide (TCO)\electron transport material (ETM)\absorber (CH₃NH₃PbI₃)\hole transport material (HTM)\Au [8–10]. Inverted perovskite solar cells have advantages such as negligible hysteresis (a phenomenon generally observed in PSC) and ease of fabrication. The optimization of the perovskite material composition might augment spectrum absorption resulting in high device performance, thus needs to be investigated with great scientific interest.

* Corresponding author.

E-mail addresses: pranay.ranjan@iitj.ac.in (P. Ranjan), er.atul89@gmail.com (A. Kumar).

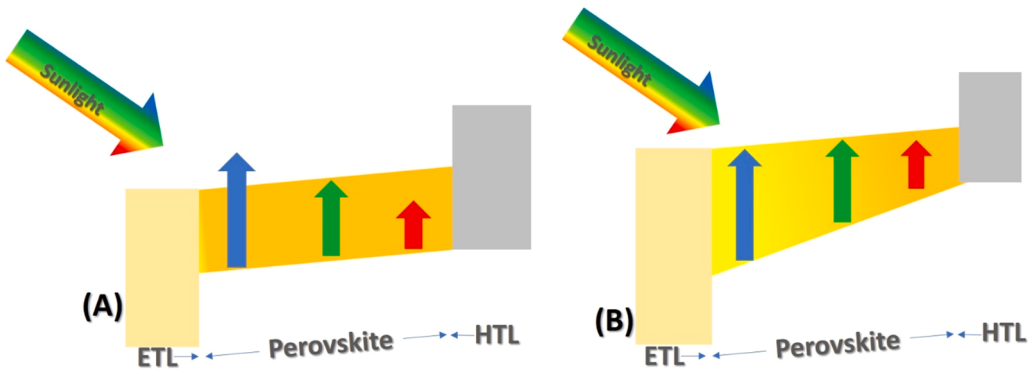


Fig. 1. (a) The inverted planar *p-i-n* perovskite solar cell with a constant bandgap. The constant bandgap has non-absorption and thermalization loss as marked by the red and blue arrows. (b) The bandgap graded perovskite layer has efficient absorption of a photon. The variable energy photons marked by red, green, and blue arrows are efficiently absorbed.

In this regard, bandgap engineering of perovskite materials enables wide absorption of the spectrum. Moreover, a range of different bandgaps is obtained by compositional engineering of ABX_3 perovskite semiconductors, where methylammonium (MA) [11,12], formamidinium (FA) [13], and Caesium (Cs) [14] are commonly utilized as monovalent A-cations within the perovskite lattice. In addition, higher bandgap perovskite absorbers have been realized through halide alloying. [15] Contemporary literature demonstrated the potential to obtain desired absorption onsets in hybrid perovskites by [16] alloying of metal halide perovskites. In the present study, we proposed a configuration of PSC employing its wide bandgap tuneability to numerically examine PCE performance. We compared the experimental device performance metrics such as the power conversion efficiency, the short circuit current, fill-factor (FF), and the open-circuit voltage of single-junction devices as a function of the bandgap profile of the perovskite absorber to assess various grading configurations to achieve PCE beyond SQ limit. Moreover, we have analyzed and highlighted the performance enhancement in engineering hybrid perovskite-based solar cell device technology for bandgap tunability via compositional grading. **Section 2** comprehensively explains the proposed device configuration and the utilized modeling approach, and **Section 3** deals with the analysis of the various bandgap grading configuration and an optimized bandgap profile resulting in optimal efficiency.

2. Guidelines for bandgap graded solar cells

The schematic of the inverted planar *p-i-n* configuration of the PSC device with a single uniform bandgap throughout its thickness is shown in Fig. 1(a). A solar cell device with a single bandgap could only absorb photons of energy greater than or equal to the bandgap of the absorber layer material. Conversely, a variable bandgap absorber could efficiently utilize the spectrum as shown in Fig. 1(b), reducing the thermalization and non-absorption losses in the device. [17,18] This would lead to a higher J_{SC} value resulting in efficiency beyond the SQ limit. The schematic of the bandgap graded *p-i-n* configuration of the perovskite device is shown in Fig. 1(b). The optimal band gap grading addresses the major losses in SQ limit i.e., thermalization and non-absorption, and could harvest all the visible region photons that are incident on the device. [19] Thermalization and non-absorption are the major losses in the detailed balance limit, combinedly responsible for 50% loss. Thus, rectifying them will result in a device with about 50% efficiency. [20] Seeing these advantages, bandgap grading is experimentally attempted in perovskite absorbers showing absorption and carrier collection enhancement. The position-dependent bandgap has an in-built electric field that will have directional carrier drift thus resulting in higher carrier mobility, reduced recombination velocity, and higher carrier collection. [21] For carrier collection enhancement, if the bandgap profile is considered at the two ends as 1 eV and 2 eV respectively, it provides an inbuilt slope $\Delta E_c = 1 \text{ eV}$, assuming the length of the absorber to be $0.6 \mu\text{m}$ in linearly graded perovskite layer, the quasi-electric field ($\epsilon = \Delta E_c / \Delta X$) caused by grading ($\Delta E_c = 1 \text{ eV}$) will be approximately around 10^6 eV/m . This additional drift field is favorable for carrier collection at the hetero-junction and lowers the electron-hole recombination in the bulk absorber. The proposed bandgap graded design will have a new effective recombination velocity for carriers in the engineered device ($S_{n \text{ eff}}$), which can be estimated from.

$$S_{n \text{ eff}} = S_n - \mu_n \epsilon$$

where μ_n is the electron mobility, S_n represents the recombination velocity of the conventional design and ϵ is the electric field that occurred from the use of the graded band-gap profile given by Ref. [21].

With variable bandgap at the front and rear of the absorber layer, the absorption co-efficient will change with the bandgap is given by $\alpha_c = A(hv - E_{g \text{ min}})^{1/2}$.

we can write an expression that is valid for the whole range of photon energies and values of b as follows.

$$\alpha_{\text{eff}} = 0 \text{ for } hv < E_{g \text{ low}}$$

$$\alpha_{\text{eff}} = 2/3(\alpha_c \text{ for } E_{g \text{ low}} / (E_{g \text{ high}} - E_{g \text{ low}})) \text{ for } E_{g \text{ low}} < hv < (3E_{g \text{ high}} - E_{g \text{ low}})/2$$

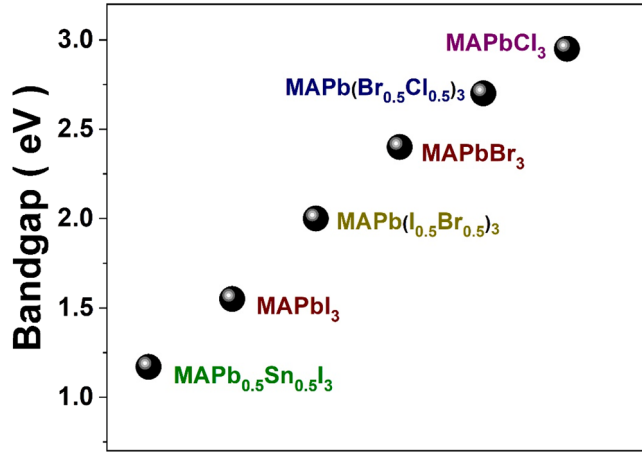


Fig. 2. The wide variation of bandgap in perovskite with variation in composition. B site variation can tune bandgap in the range from 1.17 to 1.5 eV whereas the X site variation has bandgap variation in the range 1.5–3 eV. [23,24].

Table 1

Device parameter as used in simulation [28–31].

Material parameter	FTO	SnO ₂	MAPBI ₃	Spiro-MeOTAD
Thickness (μm)	0.1	0.05	0.6	0.05
Bandgap (eV)	3.6	3.3	1.55	3
Electron affinity (eV)	4.2	4	3.9	2.45
Dielectric permittivity (eV)	9	9	6.5	3
CB effective density of states (cm^{-3})	10^{18}	$1.2 * 10^{18}$	$2.76 * 10^{18}$	$2.8 * 10^{19}$
VB effective density of states (cm^{-3})	10^{18}	$1.8 * 10^{18}$	$3.90 * 10^{18}$	10^{19}
Electron mobility (cm^2/Vs)	200	100	5	$2 * 10^{-4}$
Hole mobility (cm^2/Vs)	100	25	5	$2 * 10^{-4}$
Donor density ND (cm^{-3})	$5 * 10^{18}$	10^{18}	0	0
Acceptor density NA (cm^{-3})	0	0	$2 * 10^{13}$	10^{17}
Absorption coefficient (cm^{-1})	10^5 [33]	10^5 [32]	10^5 [33]	10^5 [33]
Defect model				
Total defect density (cm^{-3})		$8 * 10^{16}$		$5 * 10^{10}$
Defect type		Donor		Acceptor
Energetic distribution		Uniform		Uniform
Reference energy level		Above the Highest E _V		Above the Highest E _V
Capture cross section of electron (cm^2)		10^{-19}		10^{-19}
Capture cross section of hole (cm^2)		10^{-19}		10^{-19}

$$\alpha_{\text{eff}} = \alpha_c \text{ hv} < (3E_g \text{ high} - E_g \text{ low})/2$$

We have chosen the front bandgap higher as this will be advantageous for the gradual absorption of lower energy photons throughout the absorber layer. This scenario will have a quasi-electric field caused by grading in direction of the p-i-n electric field.

One of the advantages of the perovskite is the tailoring ability of its wide bandgap depending upon the composition and stoichiometry. Halide (X), Metal (B), and A site variation in ABX₃ make hybrid organo-inorganic halide perovskite MAPb(X_{1-x}X'_x)₃ a highly tunable (bandgap) material, in which the bandgap can be modulated by changing the halide, A and B composition respectively. [15,22, 23] Generally, B composition variation (by Sn doping and replacing Pb atoms), varies the bandgap from 1 to 1.5 eV, X site variation increases the bandgap from 1.5 to 3 eV [24]. Thus, providing a practically feasible way for bandgap adjustment by incorporating doping. [25,26] The empirical dependence of bandgap on each site composition is shown below. For X (halide) site variation [24].

$$E_g(x) = E_g[ABX_3] + x(E_g[ABX'_3] - E_g[ABX_3]) + bx^2$$

For B (metal) site variation [30].

$$E_g(x) = (1-x)E_g[ABX_3] + xE_g[AB'X_3] - bx(1-x)$$

The relation between the bandgap (E_g) and the composition of the perovskite based on the formula of Cs_aFA_bMA_(1-a-b)Pb(Cl_xBr_yI_(1-x-y))₃ is given below [27].

$$E_g = 1.587 - 0.039a - 0.102b + 1.543x + 0.669y$$

Where a, b are compositions for A site variation, x, y are compositions of doped halide. If we considered only halide doping leaving A and B cations of perovskite constant, then the eq. reduces to E_g = 1.587 + 0.669 y (where y is the doping concentration of bromine).

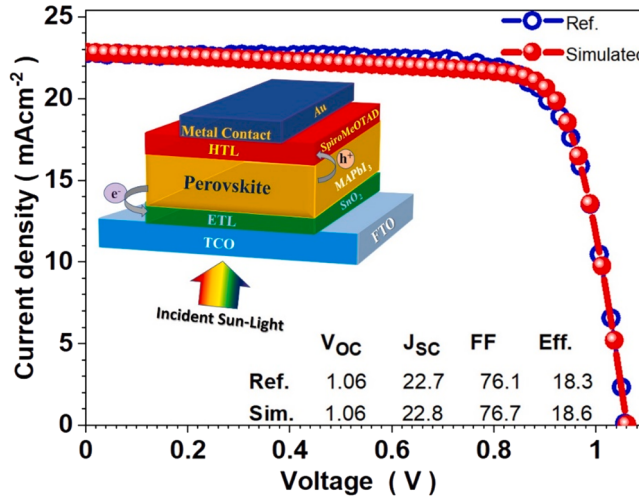


Fig. 3. The J-V plot for our simulated device (as marked by spheres) benchmarked with the experimental device (as marked by an open circle) taken from reference [17]. Inset shows the schematic of inverted-planar/superstate perovskite solar cell (*p-i-n* configuration) as utilized in simulation.

The bandgap engineering is reported for perovskite via composition variation of Sn and Br in $\text{MASn}_x\text{Pb}_{1-x}(\text{Br}_x\text{I}_{1-x})_3$. We have obtained various stoichiometry by varying the composition (x, y) in the perovskite absorber layer with the bandgap range from 1 to 2 eV. The wide variation of bandgap (from 1 to 3 eV) in perovskite with variation in B site and X site is shown in Fig. 2. Table 1.

3. Proposed configuration and modeling approach

A planar heterojunction halide PSC is replicated theoretically by employing a solar cell capacitance simulator (SCAPS-1D). It solves electrostatic Poisson eq., drift-diffusion, and continuity eq. at the junction under various illumination and biasing conditions to simulate J(V), C(V), and C(f), quantum efficiency curve, band diagram, recombination current, etc. across *p-i-n* heterojunctions optoelectrical solar cell device. Applying relevant boundary conditions at the interfaces and different contacts, SCAPS solves the coupled differential equations in (Ψ, n, p) or (Ψ, E_{Fn}, E_{Fp}) .

$$J_n = -\frac{\mu_n n}{q} \frac{dE_{Fn}}{dx} \quad (1)$$

$$J_p = \frac{\mu_p p}{q} \frac{dE_{Fp}}{dx} \quad (2)$$

$$-\frac{dJ_n}{dx} - U_n + G = \frac{dn}{dt} \quad (3)$$

$$-\frac{dJ_p}{dx} - U_p + G = \frac{dp}{dt} \quad (4)$$

$$\frac{d}{dx} \left(\epsilon_0 \epsilon_r \frac{d\Psi}{dx} \right) = -q(p - n + N_D^+ - N_A^- + \frac{\rho_{def}}{q}) \quad (5)$$

where Ψ is the electrostatic potential, ϵ_0, ϵ_r is the permittivity of vacuum and semiconductor, n and p are the respective carrier density and N_D^+, N_A^- is the density of donors and acceptors, ρ_{def} is the charge density of defects, J_n, J_p is the respective electron and hole current density, E_{Fn}, E_{Fp} is the electron and hole Fermi level $\mu_{p/e}$ is the hole/electron mobility, G is the generation rate, U is the recombination rate. Eqs. 1 and 2 are the charge carrier transport, and Eqs. 3–4 are the electron- and hole-continuity equations; Eq. 5 is the Poisson equation. SCAPS can replicate experimentally observed phenomena in solar cell devices such as light soaking, impurity photovoltaic effect, multijunction, tunneling effect, J-V hysteresis, bandgap grading, etc. using appropriate conditions, defect models, script files, recorder setup, etc. We performed benchmarking of our numerical device with an experimentally reported device. [34] The simulated device has all device parameters reasonably matching with the experimental device i.e., superstate configuration of (FTO/ETL/perovskite-absorber layer/HTL). Tin Oxide (SnO_2 , bandgap of 3.3 eV) is used as an electron transport material and Spiro-OMeTAD (bandgap of 3 eV) is used as a hole transport material. In addition, methylammonium lead halide ($\text{CH}_3\text{NH}_3\text{PbI}_3$) (bandgap of 1.55 eV) is used as an absorber layer. Fluorine doped tin oxide is used as a window layer along with gold (Au) as anode contact. The initial parameters that are required to simulate the device structure in SCAPS viz., the thickness of the layers, electron affinity, density of carriers, interfacial and bulk defect density are used as reported in the previous literature and are summarized thoroughly in

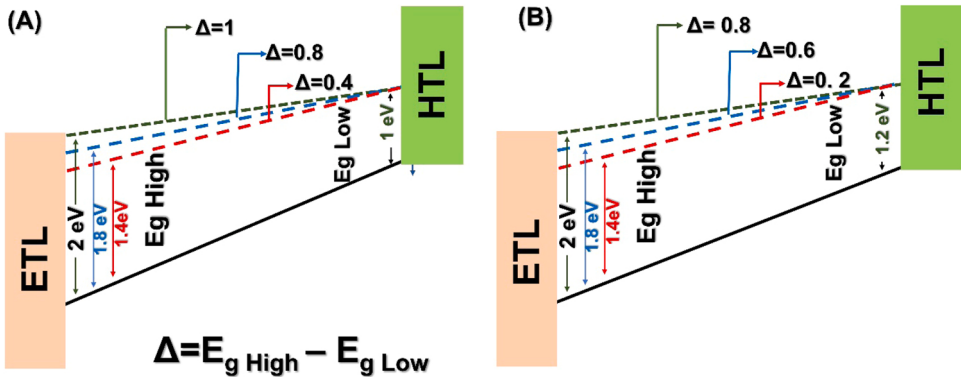


Fig. 4. (a) Schematic of bandgap grading with E_g (high bandgap) variation at a fixed rear bandgap (E_g Low) of 1 eV. (b) The schematic of bandgap grading with E_g high bandgap variation at a fixed rear bandgap (E_g Low) of 1.2 eV.

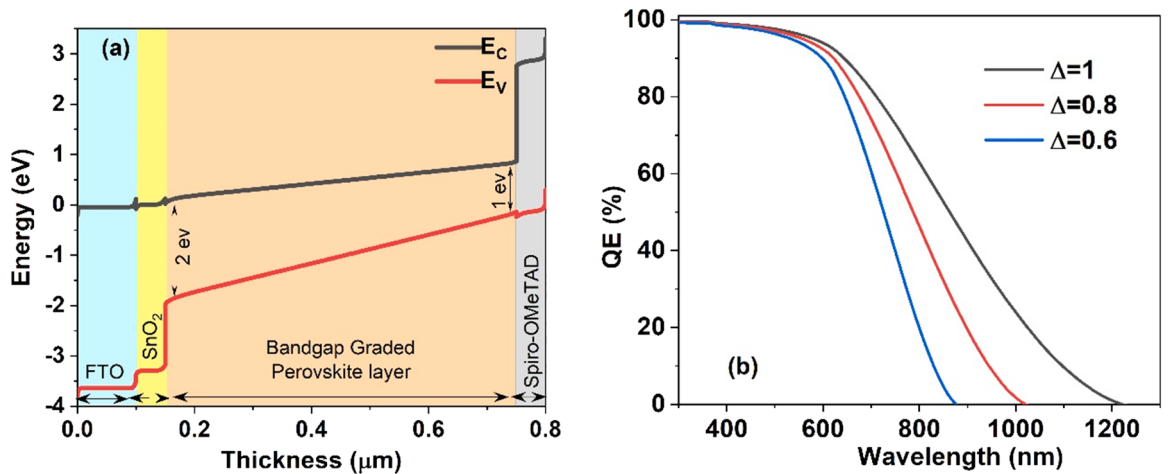


Fig. 5. (a) The simulated band diagram of bandgap graded perovskite solar cell. It shows the variable E_g throughout the absorber thickness. (b) The simulated quantum efficiency of the device. The black line shows the QE for E_g Low 1 eV and E_g high 2 eV ($\Delta = 1$; $\Delta = E_g$ High - E_g Low), and the red line shows the QE for E_g Low 1.2 eV and E_g High 2 eV ($\Delta = 0.8$), the blue line shows the QE for E_g Low 1.4 eV and E_g High 2 eV ($\Delta = 0.6$).

Table-1. Initially, we simulated the performance parameters of the device configuration as shown in the inset of Fig. 3 and matched it with an experimental device that reported an efficiency of 18%. Fig. 3 shows the J-V curve of the simulated device along with the experimental device. The overlapping of the two J-V plots reveals that the simulated device corroborates well with the experimental device. The experimental data is collated from ref. [33] by using GetData™. Our simulated device has performance parameters values, efficiency, V_{oc} , J_{sc} , and fill factor of 18%, 1.06 V, 22 mA/cm², and 76% respectively that provide the precise matching with the experimental device. In this configuration of the matched device, we have incorporated and analyzed the bandgap grading. [33–35].

4. Results and discussion

The linearly graded bandgap of perovskite solar cell, with the different slopes of absorber band levels, is represented in Fig. 4. The difference of the bandgap at the two ends is given by $E_g \text{ High} - E_g \text{ Low}$. Initially the front side of the bandgap, $E_g \text{ High}$ is fixed at 2 eV and the rear edge of the bandgap $E_g \text{ Low}$ is fixed at 1 eV. The Pb-based MAPbX₃ has a bandgap of 2 eV and Sn-based MASnX₃ has a bandgap of ~1.17 eV. We observed the differential slope of the conduction band E_C and the valence band E_V upon variation of bandgap at one of the ends while keeping fixed the other end bandgap as depicted in Fig. 4. This slope in the conduction band level provides an additional drift for photogenerated electrons in the conduction band and hole in the valence band. In addition, the highly doped HTL, ETL layer provides built-in voltage throughout the intrinsic layer and the bandgap grading provides an additional drift field. The higher bandgap can be seen toward the front, ETL which is also the illuminated side and has a gradual decrease throughout the length of the absorber. It can be concluded that the higher energy photons are absorbed in the front and the lower energy photons are absorbed in the lower bandgap end at the rear side (HTL), thus leading to maximized absorption. An efficient bandgap grading requires the front and back contact to be near ohmic contact to avoid Schottky junction formation by suitably taking suitable work functions of ETL and HTL layers.

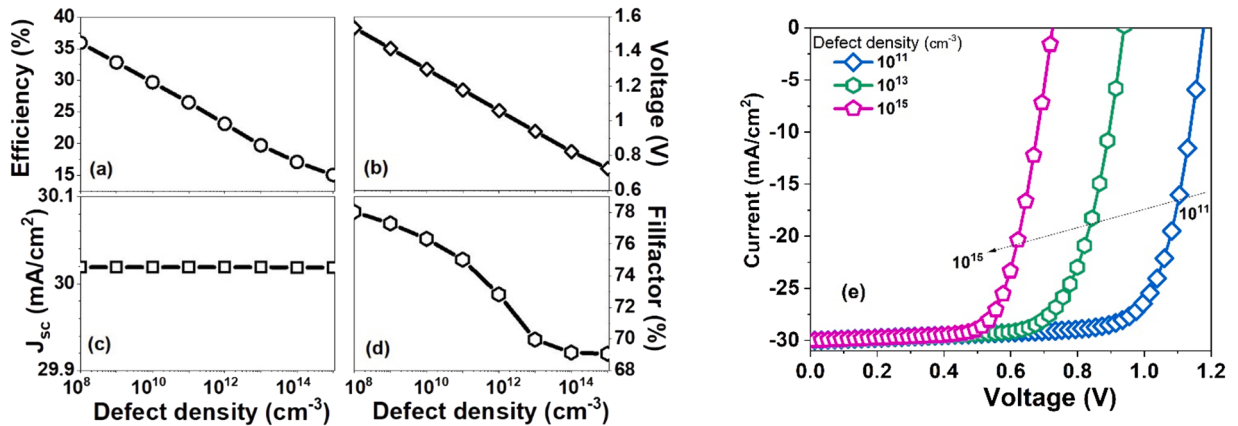


Fig. 6. (a-d) The device performance as a function of bandgap graded PSC defect density. Efficiency V_{OC} , and FF falls steeply with defects. (e) The simulated J-V curve of the bandgap graded device as a function of bulk defect density.

The various grading profiles simulated are schematically shown in Fig. 4(a-b). The rear bandgap is fixed at 1 eV and the front bandgap is varied from 2 eV – 1.4 eV in a linear fashion as schematically shown in Fig. 4(a). SCAPS can grade bandgap in various profiles such as linear, logarithmic, parabolic (two laws), power law, exponential, or any user-defined fashion. If the composition of the material is $A_{1-y}B_y$, SCAPS gives the user an option to define the properties of the pure compounds named A and B, and the composition grading $y(x)$ over the thickness of the layer: thus, defining the composition values y at the left and right side of the layer, and by specifying some grading law in between. All material properties (in our case bandgap, E_g) are then derived from the local composition parameter $y(x)$, that is, $E_g[y(x)]$ is evaluated. Linear grading laws are utilized for the composition grading $y(x)$ over a layer, as well as to set the composition dependence $E_g(y)$ of a property. Linear grading of the bandgap is given by $E_g[A(Y_B-Y)+E_g[B(Y-Y_A)/Y_B-Y_A]$.

The schematic of the slope of the conduction band and valence band in the absorber in as shown in Fig. 4(b). The rear bandgap (E_g Low) is fixed at 1.2 eV and the front bandgap is varied from 2 eV – 1.4 eV in a linear fashion. We simulate rear bandgap (E_g Low) values of 1–1.4 eV. This is to maximize absorption of incident visible photons and drift field within the absorber layer.

The simulated band diagram is shown in Fig. 5(a). This band diagram plot shows the actual slope of conduction energy level and valence band energy level, band banding profile across the perovskite layer, and interface offsets in our graded device. The quantum efficiency (QE) for the variable bandgap grading profile is simulated and shown in Fig. 5(b). The higher QE for the bandgap grading shows a higher extent of spectrum absorption i.e., higher wavelength photons, and the difference between the high and low bandgaps at the two edges of the absorber layer is marked by Δ i.e., $\Delta = E_g \text{ High} - E_g \text{ Low}$. It can be observed that the QE is different for distinct Δ values. The absorption of longer wavelength increases for different bandgap profiles depending on Δ , the wavelength range of 400–1200 nm, 400–1000 nm, and 400–880 nm for the bandgap pairs (E_g High and E_g Low) of 2–1 eV, 2–1.2 eV and 2–1.4 eV respectively. It's been observed that the absorption onset reached a maximum for the bandgap grading with a low bandgap of 1 eV (E_g Low) and a high bandgap of 2 eV (E_g High). This shows the response of wide bandgap perovskite to absorb the spectrum in the infra-red region and results in a high current generation. The quantum efficiency for the case of $\Delta = 0.6$ is in good agreement with the general experimental result in the literature, with the absorption tail positioned in 885 nm wavelength for the bandgap in the range of 1.4 eV. The bandgap of 1.4 eV corresponds to 885 nm wavelength. Similarly, the bandgap of 1.5 eV corresponds to 826 nm wavelength. This is a persistent experimental observation in literature for MAPbI_3 with bandgap of 1.4–1.55 eV. In our simulation when we took 1.4 eV bandgap in the grading profile, our QE corresponds to 880 nm which matches with the general experimental data reported previously in literature. The bandgap grading in the lower bandgap region is enhanced at the spectrum absorption and this is suitable for achieving higher short circuit current.

Fabricating a variable composition layer for achieving a graded bandgap might result in some vacancies, substitution, or interstitial bulk defects. These defects can act as a recombination center and the higher defect density may decrease the lifetime of the charge carrier and increases the recombination rate. Therefore, the advantage of bandgap grading of PSC in the absorption of the spectrum is analyzed under bulk defect density variation. The device used for Fig. 6 simulation has a bandgap grading profile of 2–1.2 eV at the two end of device. We simulated this bandgap graded configuration under the impact of absorber bulk defect in the range 10^8 cm^{-3} to 10^{15} cm^{-3} . The bandgap graded configuration shows strong sensitivity toward defect density as shown in Fig. 6(a-d). The efficiency of the bandgap graded perovskite solar cell falls linearly with increasing defect density and for the lower defect density of 10^8 cm^{-3} efficiencies is reaching nearly 35% and drop to 15% for bulk defect density of 10^{15} cm^{-3} . The presence of higher defect density leads to accelerated trapped assisted recombination and is evident by the voltage reduction to 0.8 V and by the fill factor (FF) degradation from 78% to 69% over the defect density variation of 10^8 cm^{-3} to 10^{15} cm^{-3} . There is no significant change found in the short circuit current, J_{sc} concerning the defect density variation from 10^8 to 10^{15} cm^{-3} . J_{sc} is stabilized with the increasing defect density due to robust and increased absorption by the bandgap graded absorber layer pointing toward the advantageous charge collection provided by this configuration. The experimental defect density reported in the literature for the perovskite is of the order of 10^{11} cm^{-3} . [36] J-V curve under the influence of defect density variation for the graded configuration is represented in Fig. 6. Bulk defect density in the range of

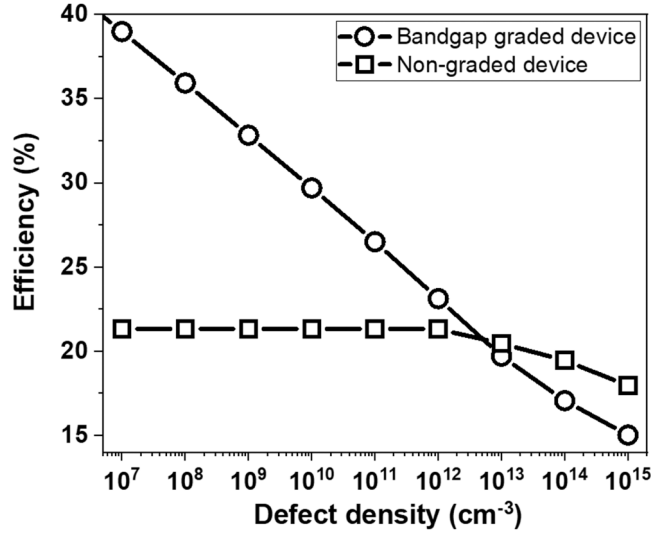


Fig. 7. The comparative performance (in presence of increasing defect density) of graded PSC and non-graded device with single bandgap of 1.5 eV.

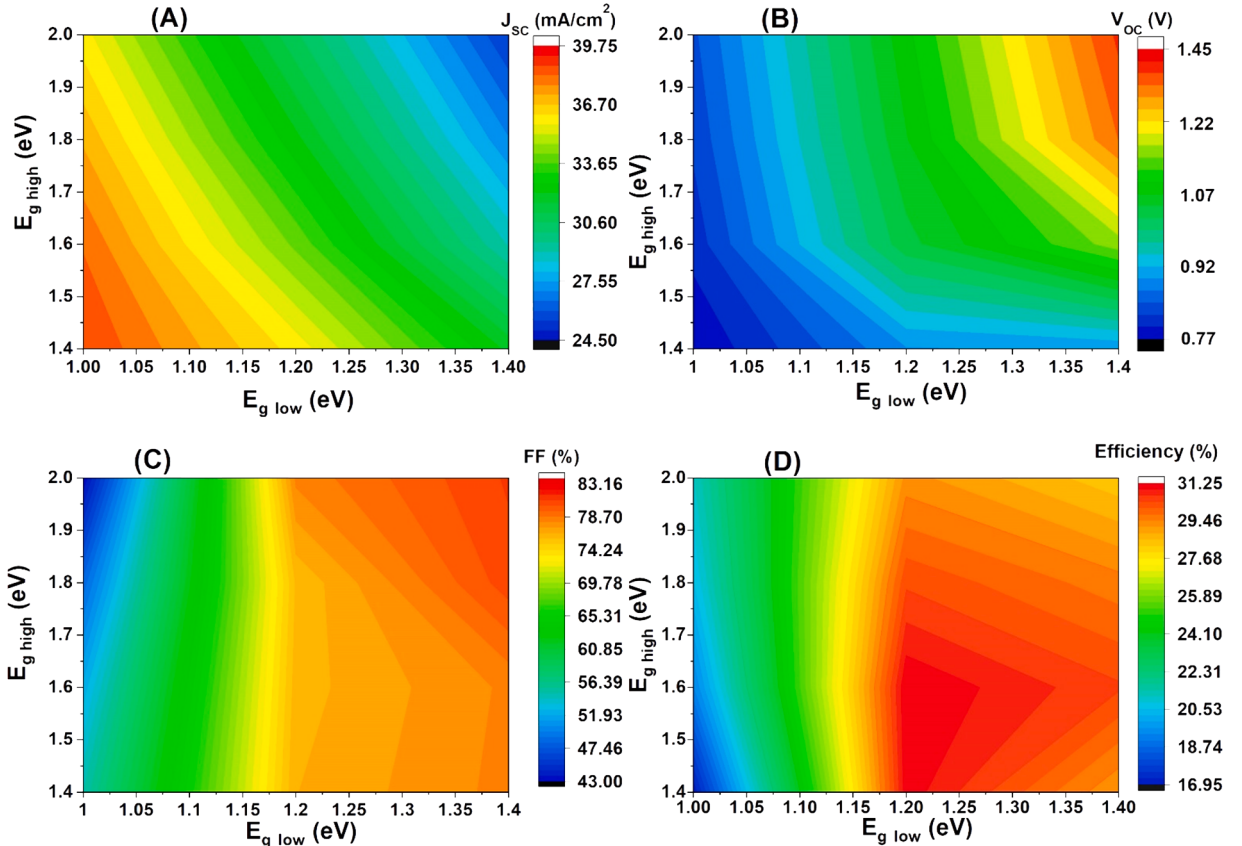


Fig. 8. (a) The simulated J_{SC} parameters of the bandgap grading device as a function of bandgap grading in the absorber layer, when the high bandgap is varied from 2 eV to 1.4 eV and the low bandgap is 1–1.4 eV. (b-d) The contour plot of efficiency, V_{OC} , FF as a function of bandgap grading, when the high bandgap is varied from 2 eV to 1.4 eV and the low bandgap is 1–1.4 eV. The efficiency maximizes in the region when $E_g \text{ High}$ is 1.4–1.6 eV and $E_g \text{ Low}$ is 1.2 eV.

Table 2

Efficiency of graded versus single bandgap PSC device.

Single bandgap PSC		Bandgap graded PSC	
Single bandgap (eV)	Efficiency (%)	Bandgap Range (eV)	Efficiency (%)
1	12.01	1–1.4	16.99
1.1	16.65	1–1.6	19.29
1.2	18.04	1–1.8	20.49
1.3	19.61	1–2	21.08
1.4	19.72	1.2–1.4	31.24
1.5	19.49	1.2–1.6	31.14
1.6	18.40	1.2–1.8	30.30
1.7	16.50	1.2–2	29.28
1.8	14.06	1.4–1.6	30.41
1.9	12.14	1.4–1.8	29.59
2	10.22	1.4–2	28.35

10^8 cm^{-3} is generally seen in crystalline silicon solar cells. The perovskites are semicrystalline and have reported defect density in the range of 10^{11} cm^{-3} to 10^{15} cm^{-3} . It can be deduced from the simulation in Fig. 6 that the density of the defect above 10^{11} cm^{-3} has a significant impact on the performance of the PSC device. Fig. 6(e) shows the simulated J-V curve for the device at various defect densities within the range 10^{11} cm^{-3} to 10^{15} cm^{-3} .

A comparison of nongraded device and bandgap graded device under the influence of increasing defect density is shown in Fig. 7. It is observed that the high efficiency of graded device is highly sensitive to defects. The efficiency falls from 38% to 15% under the influence of increasing defect density from 10^8 – 10^{15} cm^{-3} . For the non-graded device, the efficiency remains linear for low defect density and falls for higher defect density. At higher defect density bandgap graded device decay faster as compared to the non-graded.

To bring out the ideal profile of bandgap grading resulting in the optimal performance of the device, we optimized the bandgap grading configuration. The first configuration is shown in Fig. 4(a) where the rear bandgap is fixed at 1 eV and the front bandgap is made varied from 2 eV - to 1.4 eV. The impact of this profiling is analyzed for overall device performance. In the case of Fig. 4(b), we have fixed the rear bandgap at 1.2 eV and the wide front bandgap is varied from 2 eV to 1.4 eV. The impact of this variation is simulated, and optimized bandgap profiling is generated with optimal efficiency. We decreased the front wide bandgap and increased the lower rear bandgap to maximize the incident spectrum absorption. Fig. 8 shows the contour plot for J_{SC} and efficiency as a function of different bandgaps for E_g High (varied from 2 eV to 1.4 eV), E_g Low (varied from 1 eV to 1.4 eV). The obtained short circuit current is higher for the configuration having E_g Low bandgap is 1 eV and E_g High is 1.4 eV respectively. The lower bandgap of the absorber tends to absorb most of the incident spectrum thus resulting in a higher current. However, a lower bandgap will have lower V_{OC} output and lower FF output. An optimized bandgap profiling is required where overall efficiency maximizes. In bandgap grading, J_{SC} increase with lower Δ , however, other parameters such as V_{OC} and FF are observed to be decreasing with lowering Δ . With increasing Δ ie E_g High - E_g Low, the conduction band slope (dE_C/dX) increases. For $\Delta = 1$, (E_g High= 2, E_g Low=1) the slope is highest, but the J_{SC} values are not optimal, thus efficiency is not maximum for such large bandgap grading. In grading configuration efficiency is a trade-off between two competing parameters J_{SC} (required low bandgap), V_{OC} (require high bandgap), and FF (require high bandgap). A higher slope of grading might give a higher drifts field for higher Δ , but limits J_{SC} values as seen in Fig. 8(a). Thus, the bandgap at two ends of the absorber should be such that J_{SC} and V_{OC} should be optimal, and efficiency is maximized. The contour plot in Fig. 8 is evident that at fixed E_g Low J_{SC} consistently reduces with lowering in E_g High and efficiency maximizes in a narrow region where E_g low values are approximately 1.2 eV and E_g High values of 1.4 eV. The optimal pair of bandgaps at the two ends achieving best efficiency and leading to optimal bandgap grading is E_g High - E_g Low = 1.4–1.2 eV i.e a $\Delta = 0.2$ eV. This small value of the slope is achieving optimal efficiency as this value is achieving the best tradeoff among various competing factors. A higher power conversion efficiency of 31% has been observed for the bandgap grading from 1.4 to 1.2 eV, while a PCE of 21% has been observed for the bandgap grading from 2 eV to 1 eV. The perovskite absorber layer is graded from lower front bandgap to higher rear bandgap in the range 1–2 eV, the V_{oc} and FF decreased however has a considerable enhancement in the J_{sc} . Here the lower front bandgap is kept constant, and the higher rear bandgap is varied, generating a grading throughout the thickness of the absorber. With the initial bandgap grading from 2 eV to 1 eV, V_{oc} has been observed as 1.1 V and J_{sc} as 30 mA/cm². As the higher bandgap is varied from 2 eV to the lowest value of 1.4 eV for which the value of V_{oc} changes minutely but J_{sc} has recorded a considerable enhancement in its value. The efficiency of the PSC graded in this methodology has shown an increase with a decrease in the higher bandgap. Power conversion efficiency reaches as high as 31.2% for the linear bandgap profile of 1.4 eV at the front bandgap and 1.2 eV at the rear bandgap side. This increase in the efficiency of the optimized device near to SQ limit is due to the efficient absorption of the spectrum resulting in higher PCE. Table 2 summarizes the various bandgap grading ranges with their corresponding efficiencies. A comparison with the single bandgap for the benchmarked device is made to highlight the efficiency improvement in the bandgap grading scheme.

5. Conclusion

In summary, we have analyzed and numerically reproduced a high-efficiency perovskite solar cell (PSC) based on the experimentally reported efficiency of 18%. We achieved a good match with the experimental device by selecting suitable device parameters and defect models. Employing the wide bandgap tunability of perovskites, we performed bandgap grading modification to optimize the

performance of the matched or benchmarked device. A single bandgap absorber is suboptimal for spectrum matching thus a variable bandgap with superior spectrum matching and high carrier collection is proposed to obtain efficiency matching SQ limit. We analyzed the important parameters that affect this bandgap grading. The bulk defect density and bandgap grading profile are crucial, to have any net improvement in efficiency. A defect density lower than 10^{11} cm^{-3} is required for foreseeable efficiency gain. Different bandgap profiling scenarios, bandgap ranges, and slopes of conduction band were compared for their impact on device parameters. Simulations have exhibited that a high range of bandgap tunability is not essential for maximum efficiency. Rather, a well-optimized small range bandgap variation from 1.4 eV to 1.2 eV at the two ends of the absorber results in 31.2% for PCE.

Declaration of Competing Interest

The authors, declare no conflict of interest.

Acknowledgment

Authors heartily acknowledge Professor Marc Burgelman, Gent University, Belgium for providing SCAPS 1D. PR would like to acknowledge the SEED grant given by IIT Jodhpur.

References

- [1] C.A. Wadia, A. Paul, Daniel M. Kammen, Materials availability expands the opportunity for large-scale photovoltaics deployment, *Environ. Sci. Technol.* 43 (6) (2009) 2072–2077, <https://doi.org/10.1021/es8019534>.
- [2] M.M.T. Lee, Tsutomu Miyasaka, Takuro N. Murakami, Henry J. Snaith, Efficient hybrid solar cells based on meso-superstructured organometal halide perovskites, *Science* 338 (6107) (2012) 643–647, <https://doi.org/10.1126/science.1228604>.
- [3] D.W. Wang, Matthew, Elumalai, Kumar Naveen, Ashraf Uddin, Stability of perovskite solar cells, *Sol. Energy Mater. Sol. Cells* vol. 147 (2016) 255–275, <https://doi.org/10.1016/j.solmat.2015.12.025>.
- [4] C.B. Zuo, J. Henk, Hongwei Han, Jinsong Huang, David Cahen, Ding Liming, Advances in perovskite solar cells, *Adv. Sci.* 3 (7) (2016), 1500324, <https://doi.org/10.1002/advs.201500324>.
- [5] M.A.H.-B. Green, Anita, Henry J. Snaith, The emergence of perovskite solar cells, *Nat. Photonics* 8 (7) (2014) 506–514, <https://doi.org/10.1038/nphoton.2014.134>.
- [6] M.K.B. Assadi, S, R. Saidur, Hanaei H, Recent progress in perovskite solar cells, *Renew. Sustain. Energy Rev.* 81 (2018) 2812–2822, <https://doi.org/10.1016/j.rser.2017.06.088>.
- [7] W.Q. Shockley, J. Hans, Detailed balance limit of efficiency of p-n junction solar cells, *J. Appl. Phys.* 32 (3) (1961) 510–519, <https://doi.org/10.1063/1.1736034>.
- [8] Q.J. Zhou, Debaob, Fu Kailiang, Wu Xiaojie, Chen Yongsheng, Li Jingxiao, Shi-e Yang, Two-dimensional device modeling of $\text{CH}_3\text{NH}_3\text{PbI}_3$ based planar heterojunction perovskite solar cells, *Sol. Energy* 123 (2016) 51–56, <https://doi.org/10.1016/j.solener.2015.11.009>.
- [9] Pranay Ranjan Atul Kumar, Computational analysis of chalcogenides as an inorganic hole transport layer in perovskite solar cells, *Opt. Quantum Electron.* 53 (9) (2021) 1–15, <https://doi.org/10.1007/s11082-021-03186-2>.
- [10] B.S. Sengar, V. Garg, A. Kumar, P. Dwivedi, Numerical simulation: design of high-efficiency planar p-n homojunction perovskite solar cells, *IEEE Trans. Electron Devices* 68 (5) (2021) 2360–2364, <https://doi.org/10.1109/TED.2021.3066454>.
- [11] T.J.C.-B. Jacobsson, Juan-Pablo, Pazoki, Meysam, Saliba Michael, Schenck Kurt, Gratzel Michael, Hagfeldt Anders, Exploration of the compositional space for mixed lead halogen perovskites for high efficiency solar cells, *Energy Environ. Sci.* 9 (5) (2016) 1706–1724, <https://doi.org/10.1039/C6EE00030D>.
- [12] P.G. Fedeli, Francesco Callestani, Davide Ferro, Patrizia Besagni, Tullio Zappettini, Andrea Callestani, Gianluca Marchi, Enrico Ceroni, Paola Mosca, Roberto, Influence of the synthetic procedures on the structural and optical properties of mixed-halide (Br, I) perovskite films, *J. Phys. Chem. C.* 119 (37) (2015) 21304–21313, <https://doi.org/10.1021/acs.jpcc.5b03923>.
- [13] N.J.N. Jeon, Jun Hong, Yang Woo Seok, Kim Young Chan, Seungchan Ryu, Seo Jangwon, Seok Sang Il, Compositional engineering of perovskite materials for high-performance solar cells, *Nature* 517 (7535) (2015) 476–480, <https://doi.org/10.1038/nature14133>.
- [14] L. Le, "Investigation on Stability of Cesium Lead Bromide quantum dots," <http://lup.lub.lu.se/student-papers/record/8887320> 2016.
- [15] J.H.I. Noh, Sang Hyuk, Heo Jin Hyuck, Mandal Tarak N, Seok Sang Il, Chemical management for colorful, efficient, and stable inorganic–organic hybrid nanostructured solar cells, *Nano Lett.* 13 (4) (2013) 1764–1769, <https://doi.org/10.1021/nl400349b>.
- [16] Guorui Cao Mingzhe Zhu, Zhongmin Zhou, Recent progress toward highly efficient tin-based perovskite (ASnX_3) solar cells, *Nano Sel.* 2 (6) (2021) 1023–1054, <https://doi.org/10.1002/nano.202000249>.
- [17] Jakapan Chantana Yu Kawano, Takahito Nishimura Takayuki Negami, Takashi Minemoto Abdurashid Mavlonov, Theoretical impacts of single band gap grading of perovskite and valence band offset of perovskite/hole transport layer interface on its solar cell performances, *Sol. Energy* 231 (2022) 684–693, <https://doi.org/10.1016/j.solener.2021.11.072>.
- [18] A.D.Thakur Atul Kumar, Impurity photovoltaic and split spectrum for efficiency gain in $\text{Cu}_2\text{ZnSnS}_4$ solar cell, *Optik* 238 (2021), 166783, <https://doi.org/10.1016/j.jileo.2021.166783>.
- [19] Arturo Morales-Acevedo, "A simple model of graded band-gap CIGS solar cells, *Energy Procedia* 2 (2010) 169–176, <https://doi.org/10.1016/j.egypro.2010.07.024>.
- [20] Luque Antonio, Will we exceed 50% efficiency in photovoltaics, *J. Appl. Phys.* 110 (2011), 031301, <https://doi.org/10.1063/1.3600702>.
- [21] A. Morales-Acevedo, Variable band-gap semiconductors as the basis of new solar cells, *Sol. Energy* 83 (9) (2009) 1466–1471, <https://doi.org/10.1016/j.solener.2009.04.004>.
- [22] Dianxing Ju, Yangyang Dang, Zonglong Zhu, Hongbin Liu, Chu-Chen Chueh, Xiaosong Li, Lei Wang, Xiaobo Hu, Alex K.-Y. Jen, Xutang Tao, Tunable band gap and long carrier recombination lifetime of stable mixed $\text{CH}_3\text{NH}_3\text{Pb}_{x}\text{Sn}_{1-x}\text{Br}_3$ single crystals, *Chem. Mater.* 30 (5) (2018) 1556–1565, <https://doi.org/10.1021/acs.chemmater.7b04565>.
- [23] O. Ergen, S.M. Gilbert, T. Pham, S.J. Turner, M.T.Z. Tan, M.A. Worsley, A. Zettl, Graded bandgap perovskite solar cells, *Nat. Mater.* 16 (2017) 522–525, <https://doi.org/10.1038/nmat4795>.
- [24] G.M.Z. Dalpian, Xin-Gang, Kazmerski Lawrence, Zunger Alex, Formation and composition-dependent properties of alloys of cubic halide perovskites, *Chem. Mater.* 31 (7) (2019) 2497–2506, <https://doi.org/10.1021/acs.chemmater.8b05329>.
- [25] Y.Y. Liu, Zhou, Cui Dong, Ren Xiaodong, Jiankun Sun, Liu Xiaojing, Zhang Jingru, Wei Qingbo, Fan Haibo, Fengyang Yu, Fengyang and others, "Two-inch-sized perovskite $\text{CH}_3\text{NH}_3\text{PbX}_3$ (X= Cl, Br, I) crystals: growth and characterization, *Adv. Mater.* 27 (35) (2015) 5176–5183, <https://doi.org/10.1002/adma.201502597>.
- [26] Y.L. Li, Yao, Xiaomin Huo, Dong Wei, Juan Meng, Dong Jie, Bo Qiao, Suling Zhao, Zheng Xu, Dandan Song, Bandgap tuning strategy by cations and halide ions of lead halide perovskites learned from machine learning, *RSC Adv.* 11 (26) (2021) 15688–15694, <https://doi.org/10.1039/DRA03117A>.

- [27] Sneha A. Kulkarni, Tom Baikie, Pablo P. Boix, Natalia Yantara, Nripan Mathews, Subodh Mhaisalkar, Band-gap tuning of lead halide perovskites using a sequential deposition process, " J. Mater. Chem. A 2 (2014) 9221–9225, <https://doi.org/10.1039/C4TA00435C>.
- [28] S. Karthick, S. Velumani, J. Bouclé, Experimental and SCAPS simulated formamidinium perovskite solar cells: a comparison of device performance, Sol. Energy 205 (2020) 349–357, <https://doi.org/10.1016/j.solener.2020.05.041>.
- [29] E.T.S. Hoke, J. Daniel, Emma R. Dohner, Andrea R. Bowring, Karunadasa, I. Hemamala, McGehee, D. Michael, Reversible photo-induced trap formation in mixed-halide hybrid perovskites for photovoltaics, Chem. Sci. 6 (2015) 613–617, <https://doi.org/10.1039/C4SC03141E>.
- [30] R. RafieeRad, B.A. Ganji, Efficiency improvement of perovskite solar cells by utilizing CuInS₂ thin layer: modeling and numerical study, IEEE Trans. Electron Devices 68 (10) (2021) 4997–5002, <https://doi.org/10.1109/TED.2021.3102536>.
- [31] Y.B. Gan, Xueguang, Liu Yucheng, Qin Binyi, Li Qingliu, Qubo Jiang, Mo Pei, Numerical investigation energy conversion performance of tin-based perovskite solar cells using cell capacitance simulator, Energies 13 (22) (2020) 5907, <https://doi.org/10.3390/en13225907>.
- [32] M. Tagreed, Al-Saadi, H. Bushra, Hussein, B. Alaa, A.A.Shehab Hasan, Study the structural and optical properties of Cr doped SnO₂ nanoparticles synthesized by sol-gel method, Energy Procedia 157 (2019) 457–465, <https://doi.org/10.1016/j.egypro.2018.11.210>.
- [33] Kumar Atul, Numerical modeling of ion-migration caused hysteresis in perovskite solar cells, Opt. Quantum Electron. 53 (2021) 166, <https://doi.org/10.1007/s11082-021-02806-1>.
- [34] M.B.X. Johansson, Ling, Kim Byeong Jo, Thyr Jakob, Kandra Timo, Johansson, M.J. Erik, Gthelid Mats, Edvinsson Tomas, Boschloo Gerrit, Highly crystalline MAPbI₃ perovskite grain formation by irreversible poor-solvent diffusion aggregation, for efficient solar cell fabrication, Nano Energy 78 (2020), 105346, <https://doi.org/10.1016/j.nanoen.2020.105346>.
- [35] M. Burgelman, P. Nollet, S. Degrave, Modelling polycrystalline semiconductor solar cells, Thin Solid Films 361–362 (2000) 527–532, [https://doi.org/10.1016/S0040-6090\(99\)00825-1](https://doi.org/10.1016/S0040-6090(99)00825-1).
- [36] A.S.J. Chouhan, Naga Prathibha, Avasthi Sushobhan, Effect of interface defect density on performance of perovskite solar cell: correlation of simulation and experiment, Mater. Lett. 221 (2018) 150–153, <https://doi.org/10.1016/j.matlet.2018.03.095>.